

SCIENTIFIC REPORTS

OPEN

Temperature Dependence of the Dielectric Function of Monolayer MoSe₂

Han Gyeol Park¹, Tae Jung Kim², Farman Ullah³, Van Long Le¹, Hoang Tung Nguyen¹, Young Soo Kim³ & Young Dong Kim¹

The dielectric function $\epsilon = \epsilon_1 + i\epsilon_2$ of monolayer molybdenum diselenide (MoSe₂) is obtained and analyzed at temperatures from 31 to 300 K and at energies from 0.74 to 6.42 eV. The sample is a large-area, partially discontinuous monolayer (submonolayer) film of MoSe₂ grown on a sapphire substrate by selenization of pulsed laser deposited MoO₃ film. Morphological and optical characterizations verified the excellent quality of the film. The MoSe₂ data were analyzed using the effective medium approximation, which treats the film and bare substrate regions as a single layer. Second derivatives of ϵ with respect to energy were numerically calculated and analyzed with standard lineshapes to extract accurate critical-point (CP) energies. We find only 6 CPs for monolayer MoSe₂ at room temperature. At cryogenic temperatures 6 additional structures are resolved. The separations in the *B*- and *C*-excitonic peaks are also observed. All structures blue-shift and sharpen with decreasing temperature as a result of the reducing lattice constant and electron-phonon interactions. The temperature dependences of the CP energies were determined by fitting the data to the phenomenological expression that contains the Bose-Einstein statistical factor and the temperature coefficient.

Over the last few years, knowledge of two-dimensional (2-D) materials has rapidly expanded due to the enormous interest in nanotechnology and various unique physical and chemical properties based on dimensionality¹. Group-VI transition-metal dichalcogenides (TMDs) are 2-D and MX₂ materials, where M is a group-VI transition metal element (Mo or W) and X a chalcogen (S, Se, or Te). Common structural phases of TMDs include trigonal prismatic (2*H*) and octahedral (1*T*) coordinations of the metal atoms. Both phases form X-M-X layered structures coupled by weak van der Waals forces. This enables the fabrication of films of atomic thicknesses down to monolayers².

TMDs are semiconducting materials, as opposed to graphene, which is metallic. Their bandgaps are tunable depending on the number of layers, tensile strain, and external electric field^{3–5}. In addition most TMDs show a crossover from an indirect bandgap at multilayers to a direct bandgap at monolayers^{3,6–8}. In particular, molybdenum diselenide (MoSe₂) is a promising substitute for traditional semiconductors at the leading edge of research and technology for waveguiding, superconducting, and photodetecting devices^{9–11}. The spin splitting of monolayer MoSe₂ at the valence band maximum is larger than that of monolayer MoS₂, making MoSe₂ potentially useful for spintronic devices³.

The applications mentioned above are closely related to the dielectric properties of these materials. Spectroscopic ellipsometry (SE) is a precise and highly sensitive method for obtaining dielectric function data $\epsilon = \epsilon_1 + i\epsilon_2$ ¹². Several workers have reported dielectric functions of monolayer MoSe₂ using SE at room or high temperature, but these spectra are broad and transition peaks difficult to resolve^{13,14}. To reduce thermal broadening, enhance weak features, and improve resolution, data must be obtained at cryogenic temperatures^{15–17}. Furthermore, temperature dependences are needed to fully understand the working principles of devices and to properly design them for applications¹⁸. Although absorption data from 77 to 300 K in the energy region of the *A*- and *B*-excitonic peaks have been published, a systematic analysis of ϵ of monolayer MoSe₂ from cryogenic to room temperature has not been reported^{18,19}.

¹Department of Physics, Kyung Hee University, Seoul, 02447, Republic of Korea. ²Center for Converging Humanities, Kyung Hee University, Seoul, 02447, Republic of Korea. ³Department of Physics and Energy Harvest Storage Research Center (EHSRC), University of Ulsan, Ulsan, 44610, Republic of Korea. Correspondence and requests for materials should be addressed to T.J.K. (email: tjkim@khu.ac.kr) or Y.S.K. (email: yskim2@ulsan.ac.kr) or Y.D.K. (email: ydkim@khu.ac.kr)

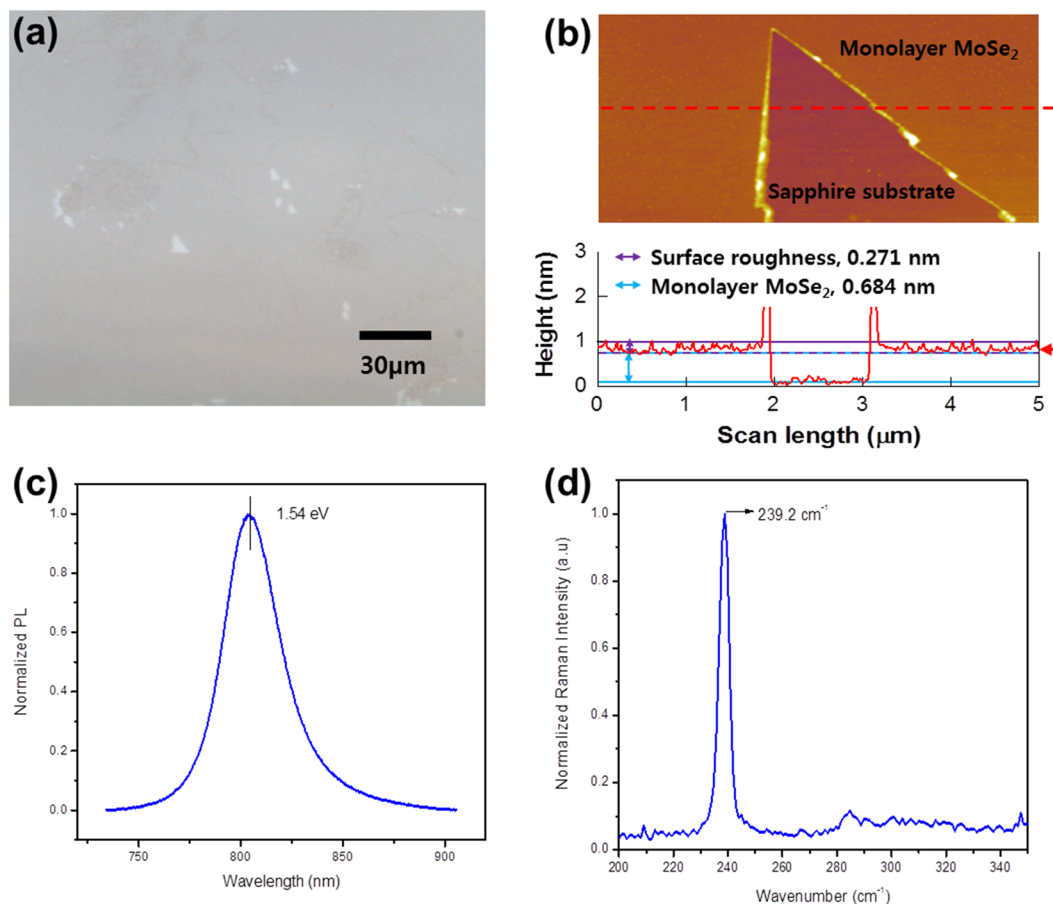


Figure 1. (a) OM image, (b) AFM image with thickness profile on red dashed line (inset), (c) PL spectrum, and (d) Raman spectrum of monolayer MoSe₂ film deposited on the polished side of a sapphire substrate.

Here, we report ε data for monolayer MoSe₂ from 0.74 to 6.42 eV at temperatures from 31 to 300 K. The sample was a large area (15 × 15 mm²) submonolayer MoSe₂ film grown by selenization of MoO₃ film that was deposited on the polished side of a sapphire substrate using pulsed laser deposition (PLD). Data were obtained by SE and analyzed using the Bruggeman effective medium approximation (EMA)²⁰. Standard lineshape analysis was done using numerically calculated second derivatives of ε with respect to energy to extract accurate critical-point (CP) energies. Six CPs are observed at room temperature. Six additional CPs are found at cryogenic temperatures. The *A*-excitonic peak at 1.61 eV shows a distinct shoulder at low temperature, which is due to the negatively charged *A*-excitonic (*A*-trionic) peak^{19,21}. At 31 and 50 K, a CP is found between the *A*- and *B*-excitonic peaks. We interpret this as either a *B*-trionic peak²² or the first excited state of the *A*-exciton²³, as predicted theoretically. The separation of the *C*-excitonic peaks, which has not reported so far, results from the spin-orbit splitting of the top valence band²⁴. The CPs blue-shift and the associated features become more prominent with decreasing temperature as a result of the reduction of lattice constant and electron-phonon interactions¹⁵. The temperature dependences of the CP energies were determined by fitting the data to the phenomenological expression that contains the Bose-Einstein statistical factor and the temperature coefficient.

Results and Discussion

Synthesis and Characterizations. The procedure for preparing monolayer MoSe₂ films is described in detail elsewhere²⁵. Briefly, a krypton fluoride (KrF) excimer laser was used to deposit a thin film of MoO₃ on the polished side of a sapphire substrate. The monolayer MoSe₂ film was obtained by selenization of MoO₃ in a selenium-rich environment in a two-zone hot-wall furnace. The chamber pressure and temperature were set to 450 mtorr and 900 °C, respectively. A mixture of Ar and H₂ was employed as the carrier gas. A 25-min exposure ensured the conversion of MoO₃ to MoSe₂.

The MoSe₂ film was characterized by optical microscopy (OM), atomic force microscopy (AFM), photoluminescence (PL), Raman spectroscopies, and X-ray diffraction. The OM image of the film is shown in Fig. 1a. The diameters of monolayer domains are a few hundred μm. The AFM image reveals that the grown MoSe₂ film is of excellent quality with no adsorbed particles on its surface. The thickness is found to be 0.684 nm, confirming that the film is indeed a monolayer (Fig. 1b). Another hallmark of good quality is provided by the PL data. The PL intensity of semiconducting TMDs decreases exponentially with increasing thickness owing to the transition of the band gap from direct to indirect^{8,11,26}. Our film shows a strong PL peak at ~800 nm (~1.55 eV), corresponding to the *A*-exciton, which arises from the *K*-point of the Brillouin zone (Fig. 1c)²¹.

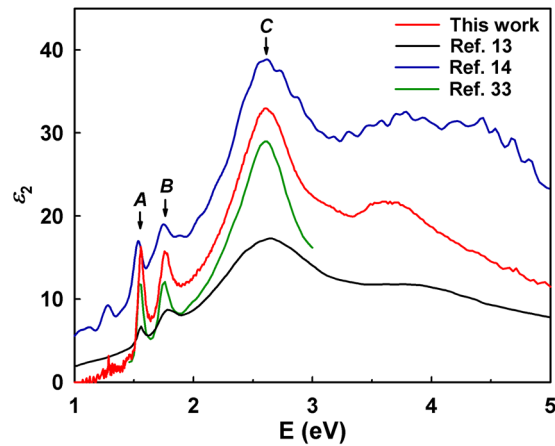


Figure 2. Imaginary parts of dielectric spectra of monolayer MoSe₂ at room temperature compared to data previously reported in refs^{13,14,33}.

The Raman spectra of monolayer MoSe₂ is given in Fig. 1d. Two main peaks associated with the A_{1g} (out of plane) and E¹_{2g} (in-plane) vibrational modes are observed at 239.2 cm⁻¹ and 285.4 cm⁻¹, respectively. The distance between the peaks, 46.2 cm⁻¹, provided additional confirmation that film is monolayer MoSe₂²⁷. Moreover, the full-width at half-maximum (FWHM) of A_{1g} is 4 cm⁻¹, indicating the highly crystalline nature of the layer²⁸.

Several research groups have determined lattice parameters of TMDs using X-ray diffraction or first principles calculations. The ratio of the lattice parameters of MoSe₂ and MoS₂ is about 1.05^{29,30}. In accordance with the ratio of lattice parameters and our previous work on MoS₂, we concluded that the monolayer MoSe₂ film is 0.693 nm thick. This agrees with thickness profile in Fig. 1b.

SE measurement and analysis at room temperature. Because SE uses relatively weak continuum light sources, mm-scale beam illumination areas are required to obtain analyzable data, which is inconsistent with the sizes of the MoSe₂ grains. Consequently, there are only a few SE studies of monolayer MoSe₂. We circumvented the size/intensity challenge using a focusing probe, as described in Methods. This allowed us to obtain spectra of domains several hundred μm in size at room temperature.

The measured pseudodielectric functions $\langle \epsilon \rangle = \langle \epsilon_1 \rangle + i \langle \epsilon_2 \rangle$ encode all sample information over the entire penetration depth of light, including not only the dielectric function of the film but also its thickness and the dielectric function of the substrate. To extract the dielectric function of the film, we used a four-phase optical model consisting of the ambient, a rough surface, the MoSe₂ monolayer, and the sapphire substrate. This is denoted here as the RT model.

The ϵ of monolayer MoSe₂ was modelled using Gaussian and Tauc-Lorentz (TL) oscillators. ϵ_2 of the Gaussian oscillator³¹ is symmetric:

$$\epsilon_{2G} = A_G e^{-\left(\frac{E-E_G}{\sigma}\right)^2}, \quad \sigma = \frac{Br}{2\sqrt{\ln(2)}}, \quad (1)$$

where A_G is the amplitude, E_G is the central energy, and Br is FWHM. ϵ_2 of the TL oscillator³² is asymmetric:

$$\begin{aligned} \epsilon_{2TL} &= \left[\frac{A_{TL} E_{TL} C (E - E_{\text{gap}})^2}{(E^2 - E_{TL}^2)^2 + C^2 E^2} \cdot \frac{1}{E} \right], \quad E > E_{\text{gap}}, \\ &= 0, \quad E \leq E_{\text{gap}}, \end{aligned} \quad (2)$$

where A_{TL} is the amplitude, E_{TL} is the central energy, C is the broadening parameter, and E_{gap} is the Tauc gap. ϵ_1 was calculated from ϵ_2 with the Kramers-Kronig integral. In general, a combination of Gaussian and TL oscillators reproduces the dielectric lineshape of monolayer MoSe₂ fairly well, but a point-by-point analysis is needed to obtain CP energies, as done below.

The dielectric spectrum of the rough-surface layer is represented in the Bruggeman EMA²⁰ modeled as a mixture of 50% monolayer MoSe₂ and 50% ambient. Our best fit to the monolayer-MoSe₂ data at room temperature yielded a 0.284 nm thickness for the rough interface. This is consistent with the AFM result in Fig. 1b.

Figure 2 compares our ϵ_2 results for a monolayer MoSe₂ domain at room temperature with previously reported data^{13,14,33}. Structureless regions at energies less than 1 eV and more than 5 eV are deleted for clarity. All data reproduce the A, B, and C features, but considerable variation is seen above 3 eV. For monolayer-scale films, such differences arise from discrepancies between the actual thickness of a film and the thickness assumed upon inverting the thin-film model. Thus thicknesses must be carefully assessed by different techniques to ensure consistency and hence accuracy, as done here. The noisy feature at 1.24 eV seems to be an artifact caused by change of detectors, as explained in Methods below.

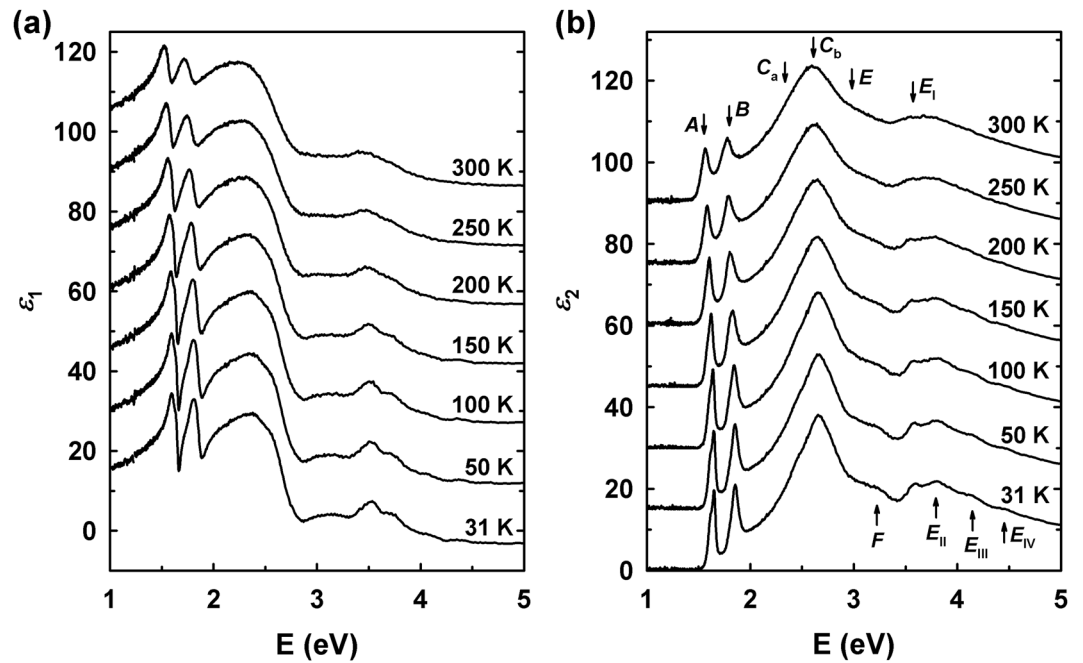


Figure 3. (a) Real and (b) imaginary parts of ϵ of monolayer MoSe₂ at temperatures from 31 to 300 K. Data from 50 K are in steps of 50 K. The spectra are offset by increments of 15 relative to the 31 K spectrum.

SE measurement and analysis at various temperatures. To acquire temperature dependences, the MoSe₂ sample was placed on a cold-finger sample holder with silver paste and sealed in an ultrahigh vacuum cryostat chamber¹⁷, as described in Methods. Condensation artifacts at low temperatures were therefore minimized. Stress-free fused-quartz windows on the chamber provided non-normal-incidence optical access to the sample³⁴. The temperature of the MoSe₂ sample was decreased to 31 K with the closed-cycle helium refrigerator. $\langle\epsilon\rangle$ was determined from 0.74 to 6.42 eV at 31 K and at 25 K intervals starting at 300 K. The data themselves were acquired with a dual-rotating-compensator SE without the focusing probe, as described in Methods. Therefore, the measured $\langle\epsilon\rangle$ for the temperature dependence study contain not only the information about the perfect monolayer domains but also of the incomplete-monolayer and substrate-exposed areas.

$\langle\epsilon\rangle$ was analyzed using a 5-phase optical model consisting of the ambient, a rough surface, the submonolayer MoSe₂ film, the sapphire substrate, and the silver paste backing. We call it TD model. We analyzed the data assuming coherent superposition for the front-surface reflection and incoherent superposition for the back-surface reflection. The back-surface contribution therefore affects the intensity not the polarization state. The back side of our substrate was unpolished, and so its contribution to the intensity is small, and the measured depolarization is less than 1.5% over the entire spectral range. The ϵ of submonolayer is modeled by Bruggeman EMA comprised of monolayer MoSe₂, the defect region, and the ambient. The ϵ of monolayer MoSe₂ is the red line in Fig. 2. The broad spectrum of the defect region was determined by averaging several measurements on incomplete MoSe₂ and MoO₃ areas using a focused beam spot (Fig. S1). The material ratio in the EMA was found to be 54.53% monolayer MoSe₂, 27.34% defect region, and 18.13% ambient. A point-by-point approach was used to extract ϵ of the monolayer MoSe₂ from the TD model. The two ϵ spectra deduced from the RT and TD models at room temperature agree well, as shown in Fig. S2. We carefully examine these dielectric spectra in next section. The point-by-point approach on TD model was applied to the other data at various temperatures with same parameters, except for the thicknesses of the MoSe₂ and roughness layers, since the film thickness decreases with temperature. We took this into consideration from literature X-ray data and first principles calculations of MoSe₂ lattice parameters^{35,36}. The ratio of thicknesses obtained by X-ray scattering at temperatures 77 K and 300 K is 1.0015, a difference of less than 0.2%, having estimated thickness of MoSe₂ layer at 31 K is 0.692 nm.

Figure 3 shows our ϵ results for monolayer MoSe₂ at temperatures from 31 to 300 K offset by increments of 15 relative to the 31 K spectrum. 10 CP structures (A, B, C_a, C_b, E, F, and E_{I-IV}) are marked in Fig. 3(b). The identification of A, B, C_a, C_b, E, and F CPs is determined by band-structure calculations. The A and B CPs, and the C_a and C_b CPs, involve transitions from the top of the valence band and its spin-orbit-split partner to the lowest conduction band at K and the X (around $\frac{2}{3}$ of Γ -K line; $\vec{k} = \frac{2}{3}(\frac{4\pi}{3a}\hat{k}_x)(m^{-1})$), respectively^{23,24}.

The main contributions of the E CP arise from multiple transitions near the $\frac{1}{2}$ K-M line ($\vec{k} = \frac{1}{2}(\frac{7\pi}{3a}\hat{k}_x - \frac{\pi}{\sqrt{3}a}\hat{k}_y)(m^{-1})$) and the X point²⁴. We find five additional CPs (F and E_{I-IV}) above 3 eV that have not yet been reported. The origin of the F CP structure might be understood as E2^{+/-} multiple transitions between Γ and K points according to ref.²⁴, since the energy difference of about 0.3 eV between the main contributions of the E and F CPs matches the difference between the E1^{+/-} and E2^{+/-} transitions in ref.²⁴, where the ‘+’ and ‘-’ symbols indicate that the transitions are split by spin-orbit interaction. Since the transition points of most CPs of monolayer MoSe₂ are fairly similar to those of MoTe₂²⁴,

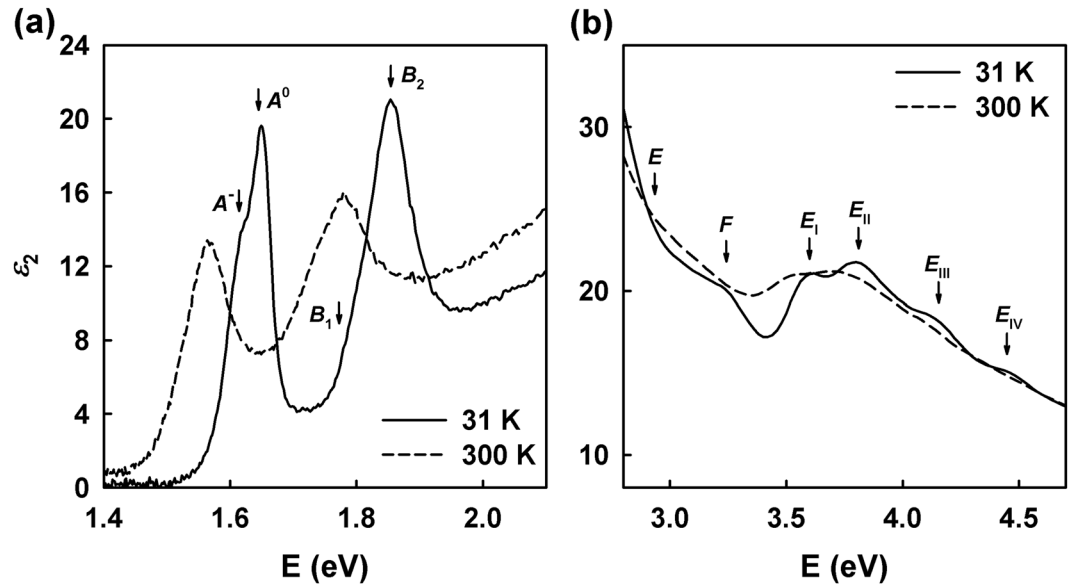


Figure 4. ϵ_2 spectra of monolayer MoSe₂ at 31 (solid line) and 300 K (dashed line) on expanded scales near regions of (a) A⁻, A⁰, B₁, and B₂ CPs and (b) E, F, and E_{I-IV} CPs.

the E_I and E_{II} CPs can be assigned to transitions around the $\frac{1}{2}$ M- Γ line or the M-point, where the G^{+/-} and H^{+/-} transitions occur in monolayer MoTe₂. Since these conjectures do not consider density-of-states and transition-probability, a further systematic theoretical investigation is needed. All CP structures blue-shift and sharpen as the temperature was lowered. This is consistent with the reduced lattice parameter and electron-phonon interaction at low temperatures¹⁵.

For detailed analysis, ϵ_2 at 31 and 300 K is plotted on expanded scales in two ranges in Figs 4a and b. A linear filtering algorithm of Savitzky and Golay (Table I of ref.³⁸, 11-point convolution) was used to highlight distinct CP structures in Fig. 4(b). The 31 K data exhibit a clear shoulder in the A exciton at about 1.6 eV. This is interpreted in temperature-dependent absorption and PL studies on monolayer MoSe₂^{19,21} to originate from a tightly bound charged exciton. The B peak shows no obvious shoulder, but has a strongly asymmetric lineshape that cannot be described by a single oscillator. A band-structure calculation of MoSe₂ anticipated another transition in the B-excitonic peak, interpreting it as the first excited state of the A exciton²³. Excited exciton states are observed in monolayer WS₂³⁷, but have not yet been reported for monolayer MoSe₂. However, another band-structure calculation on similar material of monolayer MoS₂ indicates the existence of a B-trionic peak next to the B-excitonic peak²². The identification of the B₁ CP is not yet clear because it is dominated by the huge B₂ CP. This needs to be investigated in more detail in the future.

CP Analysis. Second derivatives $\frac{d^2\epsilon}{dE^2}$ were evaluated numerically to distinguish overlapping CP structures and to determine values of CP energies. These calculations were done with a Savitzky-Golay second-derivative algorithm (Table IV of ref.³⁸, 11-point convolution) to reduce noise and minimize lineshape distortion³⁸. Regression analysis was then used to fit CP parameters to the standard analytic CP expression³⁹

$$\begin{aligned} \frac{d^2\epsilon}{d\omega^2} &= n(n-1)A_{\text{amp}}e^{i\phi}(\hbar\omega - E + i\Gamma)^{n-2}, \quad n \neq 0, \\ &= A_{\text{amp}}e^{i\phi}(\hbar\omega - E + i\Gamma)^{-2}, \quad n = 0, \end{aligned} \quad (3)$$

where A_{amp} is the amplitude, ϕ is the phase, E is the CP energy, and Γ is the broadening parameter. The exponent $n = -1$, $-\frac{1}{2}$, 0, and $\frac{1}{2}$ describes excitonic, and one-, two-, and three-dimensional CPs, respectively. In the 2-D system, $n = \frac{1}{2}$ is therefore forbidden. We simultaneously fit real and imaginary parts of $\frac{d^2\epsilon}{dE^2}$ to better define the parameters. The excitonic lineshape ($n = -1$) yields the best representation of all CPs of the monolayer material. This was also the case for MoS₂^{17,40}.

Figure 5 shows the second derivatives and their best fits at 31, 150, and 300 K. The open circles are the calculated second derivatives of ϵ_1 , and the solid and the dashed lines the best-fit results for $\frac{d^2\epsilon_1}{dE^2}$ and $\frac{d^2\epsilon_2}{dE^2}$, respectively. The data for $\frac{d^2\epsilon_2}{dE^2}$ are not shown. The number of points for $\frac{d^2\epsilon_1}{dE^2}$ was properly reduced for clarity. In the derivative spectra, CP energies blue-shift as the temperature is reduced, and the 31 K CP structures are obviously larger and sharper than those determined for higher temperatures. Near room temperature the E_{I-IV} CPs cannot be analyzed due to the low signal-to-noise ratio. Thus the high-energy region above 3.62 eV eliminated to prevent erroneous conclusions about overlapping CP.

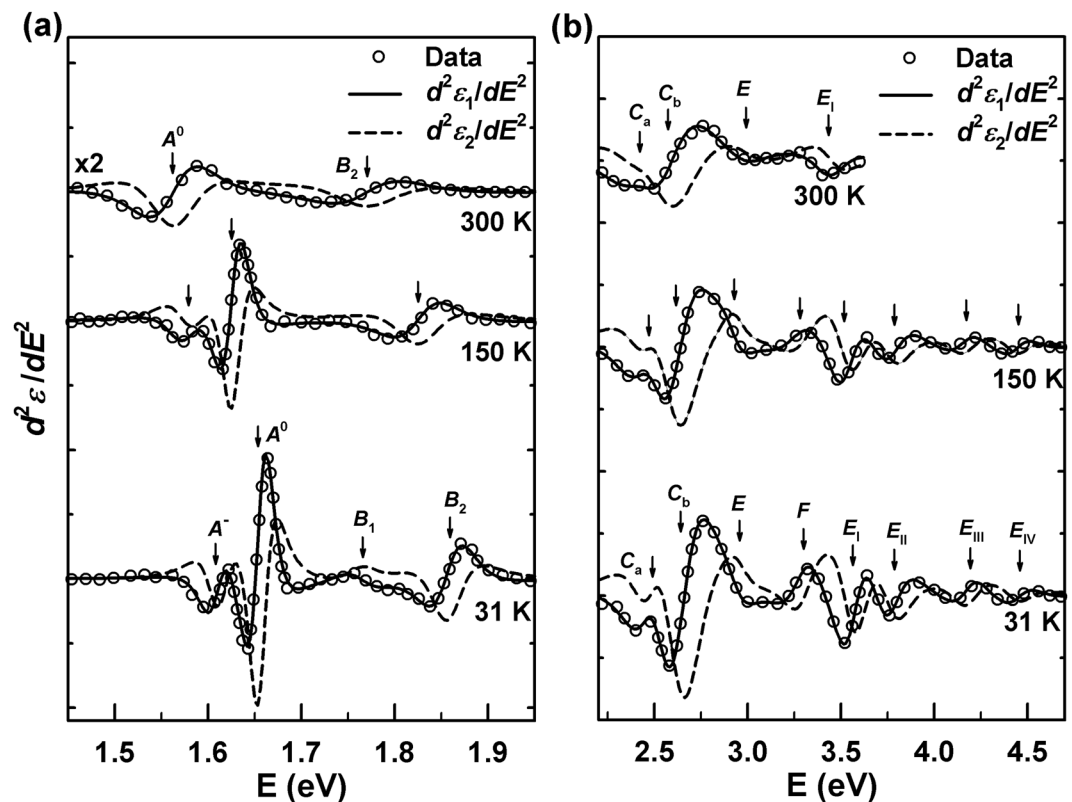


Figure 5. Second energy derivatives of ε of monolayer MoSe₂ at 31, 150, and 300 K for (a) A^- , A^0 , B_1 , and B_2 CPs and (b) C_a , C_b , E , F , and E_{I-IV} CPs. The best fits are to $\frac{d^2 \varepsilon_1}{dE^2}$ (solid lines) and $\frac{d^2 \varepsilon_2}{dE^2}$ (dashed lines). For clarity, only $\frac{d^2 \varepsilon_1}{dE^2}$ (open circles) is shown, and the number of points is appropriately reduced.

CP energies (eV)	This work		Experiment (RT)		Band Calculation	
	31 K	300 K	SE ¹³	Reflectance ³³	GW-BSE ²³	GW-BSE ²⁴
A^-	1.61	—	1.62	1.55 ^b	1.61	1.86
A^0	1.66	1.56	—	—	—	—
B_1	1.76	—	1.82	1.75	1.82 ^c	2.03
B_2	1.86	1.77	—	—	—	—
C_a	2.49	2.43	—	—	2.25 ^c	2.45
C_b	2.64	2.57	2.64 ^a	2.62 ^b	2.35 ^c	2.55
E	2.95	3.00	—	—	—	2.76 ^d
F	3.30	—	—	—	—	3.00 ^d
E_I	3.56	3.44	—	—	—	—
E_{II}	3.77	—	—	—	—	—
E_{III}	4.19	—	—	—	—	—
E_{IV}	4.46	—	—	—	—	—

Table 1. CP energies at 31 and 300 K compared to data previously reported in refs^{13,23,24,33}. ^aExtracted from Fig. 1(b) of ref.¹³. ^bExtracted from Fig. 1(i) of ref.³³. ^cExtracted from Fig. 4(c) of ref.²³. ^dExtracted from Fig. 1(c) of ref.²⁴.

The exact values of CP energies at 31 and 300 K from the best fits are listed on Table 1. Most match previously reported values^{13,23,24,33}. The B_1 and E_{I-IV} CP energies have not been reported so far.

As mentioned above, the ε from TD model was carefully compared with the result of RT model using CP analysis (Fig. S3, Table S1). The differences of 6 CP (A^- , B_2 , C_a , C_b , E , and E_I) energies at 300 K between two models are under 0.03 eV which are generally less than the differences among the reported CP energies^{13,23,24,33}.

The temperature dependences of the CPs are shown in Fig. 6. The open dots are CP energies from the regression analysis and the solid lines are best fits using either a phenomenological expression or a linear equation. A^- , A^0 , B_2 , C_a , C_b , and E_I CPs were fit with the expression that contains the Bose-Einstein statistical factor for phonons¹⁶.

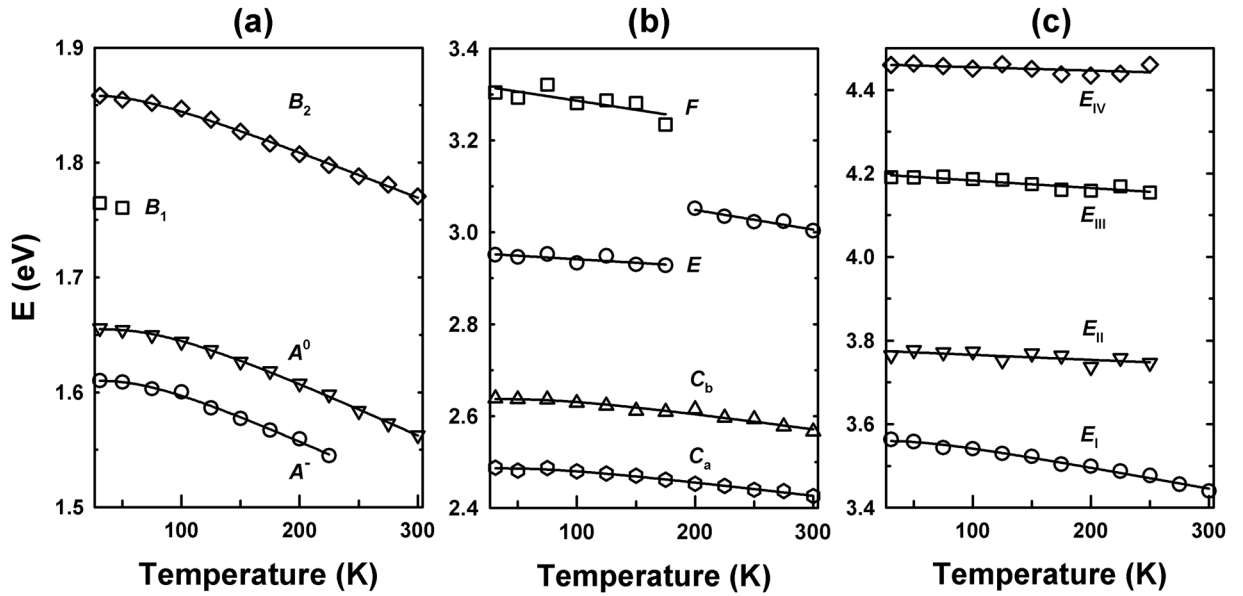


Figure 6. Temperature dependences of the CP energies (open symbols) of monolayer MoSe₂ and the best fits (solid lines) for (a) A⁻, A⁰, B₁, and B₂ CPs, (b) C_a, C_b, E, and F CPs, and (c) E_{I-IV} CPs.

CPs	E_B (eV)	a_B (meV)	Θ (K)	E_L (eV)	λ (10^{-4} eV K ⁻¹)
A ⁻	1.66	54	221	—	—
A ⁰	1.72	63	258	—	—
B ₂	1.90	39	188	—	—
C _a	2.53	42	260	—	—
C _b	2.69	52	284	—	—
E (31–175 K)	—	—	—	2.96	1.54
E (200–300 K)	—	—	—	3.13	4.30
F	—	—	—	3.33	3.96
E _I	3.61	48	183	—	—
E _{II}	—	—	—	3.78	1.20
E _{III}	—	—	—	4.20	1.82
E _{IV}	—	—	—	4.46	0.81

Table 2. Best-fit parameters for the temperature dependences of CP energies of monolayer MoSe₂.

$$E(T) = E_B - a_B \left[1 + \frac{2}{e^{\Theta/T} - 1} \right], \quad (4)$$

where E_B , a_B , and Θ , are CP energy at 0 K, strength of electron-phonon interaction, and mean frequency of phonons, respectively. E , F , and E_{I-IV} CPs were fit with the linear equation¹⁶:

$$E(T) = E_L - \lambda T, \quad (5)$$

where E_L is CP energy at 0 K and $-\lambda$ is the temperature coefficient, dE/dT . In Fig. 6a, the A⁻ and A⁰ CPs have identical lineshapes, which certifies their adjoined transition origins. These two lineshapes are in good agreement with previously reported PL results^{19,21} (Fig. S4). Though there are mismatches caused by experimental uncertainties and differences between SE and PL, they are generally less than 0.02 eV. Therefore, the temperature dependences are reliable. The temperature dependence of B₁ CP was not fit because the weak structure of B₁ CP could only be resolved from that of the B₂ CP at 31 and 50 K. As mentioned above, the E and F CPs appear to share transition points in the Brillouin zone. The relatively weak structure of the F CP was not separable from that of the E CP at temperatures above 180 K although the amplitude of the F CP is non-negligible. In Fig. 6b, the kink of the temperature dependence of E CP was caused by eliminating the overlapped F CP. Table 2 contains the best fit results with equation (4) or (5). The a_B and Θ values of A⁻ and A⁰ CPs are similar to each other, as expected from Fig. 6a. The Θ value of monolayer MoSe₂ is probably less than that of bulk MoSe₂, as expected for the Debye model in a lower dimension. Though the Θ value of bulk MoSe₂ has not been reported, we can estimate it from values of Θ for monolayer and bulk MoSe₂ that are obtained from the phenomenological expression using ellipsometric and piezoreflectance data, respectively^{17,41}. The Θ values of the A- and

B -excitonic peaks of monolayer MoS_2 ¹⁷ are about 250 K, while those of bulk MoS_2 are about 550 K⁴¹. Therefore, we expect that the Θ values for monolayer MoSe_2 given in Table 2 are physically consistent with reported values.

Conclusions

We report and analyze the intrinsic dielectric response ε of monolayer MoSe_2 , for energies from 0.74 to 6.42 eV and temperatures from 31 to 300 K. The data were obtained by SE. 6 CPs (A^0 , B_2 , C_a , C_b , E , and E_1) at 300 K and 6 additional CPs (A^- , B_1 , F , and $E_{\text{II-IV}}$) at cryogenic temperatures were observed. In particular, the appearance of separate B_1 and B_2 , and C_a and C_b CPs were expected from theoretical studies only. Numerically calculated second derivatives of ε with respect to energy were used to extract CP energies. At low temperatures, sharper structures at higher energies were observed as the result of decreased lattice constant and electron-phonon interactions. We determined the temperature dependence of each CP energy using a linear equation or a phenomenological expression that contains the Bose-Einstein statistical factor. This allows CP energies to be estimated at every temperature from 31 to 300 K. These results are helpful for understanding the optical characteristics of monolayer MoSe_2 , and to facilitate precise engineering of optoelectronic devices based on 2-D materials.

Methods

Monolayer MoSe_2 growth. The sample was prepared by PLD followed by selenization. A highly pure MoO_3 target of approximately 20 mm diameter was placed in a rotating target holder. The target was exposed to a laser beam for several minutes to remove surface contaminants. A sapphire substrate approximately $20 \times 20 \text{ mm}^2$ was placed in a rotating substrate holder. The distance between the substrate and target was 25 cm. The chamber pressure was 25 mTorr, established by flowing high pure argon (Ar) at 10 sccm. A KrF excimer laser ($\lambda = 248 \text{ nm}$, CompexPro 102 F) with 20 ns pulse width, 200 mJ/cm^2 power density, 3 Hz repetition rate deposited thin MoO_3 films in 45 s. The substrate temperature during deposition was 700 °C. The as-deposited MoO_3 films were then converted to MoSe_2 by selenization in a two-zone hot-wall furnace. Se powder (Sigma Aldrich, 99.99%) was placed in the low temperature zone at 450 °C, and the film located in the high temperature zone at 900 °C. A mixture of Ar and H_2 were employed as carrier gases to transport Se vapor from the colder to the hotter zone. H_2 also assist in reducing MoO_3 .

Characterization. PL and Raman spectra were obtained at room temperature using a diode-pumped solid-state laser (Lasos GmbH, BLK 73100 TS). Excitation was done at 473 nm with 10 mW power. The spot size of the laser was about $\sim 10 \mu\text{m}$. A three-grating monochromator (Dongwoo Optron, Monora 500i) with a focal length of 50 cm was used to analyze the light scattered from the sample. The detector was a thermoelectrically cooled Si CCD detector with a pixel matrix of 1024×244 (Andor Ultravac, iDus 420). Wavelengths were calibrated with a standard Ne calibration lamp (Newport, 6032).

Topographic images of the MoSe_2 films were obtained using the intermittent contact mode of an AFM (Asylum Research, MFD-3D) with Si tips (Olympus, AC240). The nominal normal spring constant was 2 N/m and the scan speed was 0.5 Hz.

SE. Pseudodielectric spectra of monolayer MoSe_2 domains were recorded in the ‘Isotropic + Depolarization’ mode of a M2000-FI ellipsometer (J. A. Woollam Co., Inc.) The ellipsometer was equipped with a focusing probe accessory, which reduces the diameter of beam spot from $\sim 10 \text{ mm}$ to $\sim 100 \mu\text{m}$. The measurement range is 245 to 1000 nm at 1.5 nm intervals and from 1000 to 1664 nm at 3.5 nm intervals. Light sources were xenon and quartz tungsten halogen (QTH) lamps. The detectors were two charge-coupled device (CCD) arrays. Noise occurs near 1000 nm ($\sim 1.24 \text{ eV}$), where the Si detector loses sensitivity and is replaced with an InGaAs unit. Data were obtained at angles of incidence of 55, 60, 65, and 70°. Each data point represents an average of 500 revolutions of the compensator.

For cryogenic measurements, a different ellipsometer (RC2, J. A. Woollam Co., Inc.) was employed. This ellipsometer used QTH and deuterium lamps and Si and InGaAs CCD array detectors. Data were obtained at 1 nm intervals from 193 to 1000 nm, and at 2.5 nm intervals from 1000 to 1690 nm. The AOI was 68.457° and measurements were completed in 150 seconds. The focusing probe accessory was not used in the temperature-dependent experiments due to the lack of space between the cryostat chamber and the SE.

Cryostat system. The cryostat consisted of a stainless-steel chamber with rotary and turbomolecular pumps, and operated near the 10^{-8} Torr vacuum level. The temperature of the MoSe_2 sample was regulated using a 331 Temperature Controller (Lake Shore Cryotronics, Inc.) with a heating element inside the sample holder and a silicon-diode thermometer on the corner of the sample. A closed-cycle helium refrigerator (M125 Helium Compressor, Oxford Instruments plc) was employed for decreasing the temperature.

Analysis of ε . Rough modelling of ε of monolayer MoSe_2 was carried out by the WVASE software internal to the ellipsometers (version 3.826, J. A. Woollam Co., Inc.) with Tauc-Lorentz and Gaussian oscillators. Point-by-point approach to extract precise ε of monolayer MoSe_2 and its temperature dependence was also performed with WVASE program.

Data availability. The datasets generated during and/or analyzed during the current study are available from the corresponding author on reasonable request.

References

- Gupta, A., Sakthivel, T. & Seal, S. Recent development in 2D materials beyond graphene. *Prog. Mater. Sci.* **73**, 44–126, <https://doi.org/10.1016/j.pmatsci.2015.02.002> (2015).
- Manzeli, S., Ovchinnikov, D., Pasquier, D., Yazyev, O. V. & Kis, A. 2D transition metal dichalcogenides. *Nat. Rev. Mater.* **2**, 17033, <https://doi.org/10.1038/natrevmats.2017.33> (2017).

3. Zhang, Y. *et al.* Direct observation of the transition from indirect to direct bandgap in atomically thin epitaxial MoSe₂. *Nat. Nanotechnol.* **9**, 111–115, <https://doi.org/10.1038/NNANO.2013.277> (2013).
4. He, K., Poole, C., Mak, K. F. & Shan, J. Experimental demonstration of continuous electronic structure tuning via strain in atomically thin MoS₂. *Nano Lett.* **13**, 2931–2936, <https://doi.org/10.1021/nl4013166> (2013).
5. Yuan, H. *et al.* Zeeman-type spin splitting controlled by an electric field. *Nat. Phys.* **9**, 563–569, <https://doi.org/10.1038/NPHYS2691> (2013).
6. Mak, K. F., Lee, C., Hone, J., Shan, J. & Heinz, T. F. Atomically thin MoS₂: a new direct-gap semiconductor. *Phys. Rev. Lett.* **105**, 136805, <https://doi.org/10.1103/PhysRevLett.105.136805> (2010).
7. Zeng, H. *et al.* Optical signature of symmetry variations and spin-valley coupling in atomically thin tungsten dichalcogenides. *Sci. Rep.* **3**, 1608, <https://doi.org/10.1038/srep01608> (2013).
8. Froehlicher, G., Lorchat, E. & Berciaud, S. Direct versus indirect band gap emission and exciton–exciton annihilation in atomically thin molybdenum ditelluride (MoTe₂). *Phys. Rev. B* **94**, 085429, <https://doi.org/10.1103/PhysRevB.94.085429> (2016).
9. Hu, F. *et al.* Imaging exciton–polariton transport in MoSe₂ waveguides. *Nat. Photonics* **11**, 356–360, <https://doi.org/10.1038/NPHOTON.2017.65> (2017).
10. Shi, W. *et al.* Superconductivity series in transition metal dichalcogenides by ionic gating. *Sci. Rep.* **5**, 12534, <https://doi.org/10.1038/srep12534> (2015).
11. Xia, J. *et al.* CVD synthesis of large-area, highly crystalline MoSe₂ atomic layers on diverse substrates and application to photodetectors. *Nanoscale* **6**, 8949–8955, <https://doi.org/10.1039/c4nr02311k> (2014).
12. Aspnes, D. E. Spectroscopic ellipsometry—a perspective. *J. Vac. Sci. Technol. A* **31**, 058502, <https://doi.org/10.1116/1.4809747> (2013).
13. Liu, H.-L. *et al.* Optical properties of monolayer transition metal dichalcogenides probed by spectroscopic ellipsometry. *Appl. Phys. Lett.* **105**, 201905, <https://doi.org/10.1063/1.4901836> (2014).
14. Choi, B. K. *et al.* Temperature dependence of band gap in MoSe₂ grown by molecular beam epitaxy. *Nanoscale Res. Lett.* **12**, 492, <https://doi.org/10.1186/s11671-017-2266-7> (2017).
15. Gopalan, S., Lautenschlager, P. & Cardona, M. Temperature dependence of the shifts and broadenings of the critical points in GaAs. *Phys. Rev. B* **35**, 5577–5584, <https://doi.org/10.1103/PhysRevB.35.5577> (1987).
16. Lautenschlager, P., Garriga, M. & Cardona, M. Temperature dependence of the interband critical-point parameters of InP. *Phys. Rev. B* **36**, 4813–4820, <https://doi.org/10.1103/PhysRevB.36.4813> (1987).
17. Park, H. G. *et al.* Temperature dependence of the critical points of monolayer MoS₂ by ellipsometry. *Appl. Spectrosc. Rev.* **51**, 621–635, <https://doi.org/10.1080/05704928.2016.1166436> (2016).
18. Abid, I. *et al.* Temperature-dependent plasmon–exciton interactions Au/MoSe₂ nanostructures. *ACS Photonics* **4**, 1653–1660, <https://doi.org/10.1021/acsp Photonics.6b00957> (2017).
19. Lu, X. *et al.* Large-area synthesis of monolayer and few layer MoSe₂ films on SiO₂ substrates. *Nano Lett.* **14**, 2419–2425, <https://doi.org/10.1021/nl5000906> (2014).
20. Aspnes, D. E. Optical properties of thin films. *Thin Solid Films* **89**, 249–262, [https://doi.org/10.1016/0040-6090\(82\)90590-9](https://doi.org/10.1016/0040-6090(82)90590-9) (1982).
21. Ross, J. S. *et al.* Electrical control of neutral and charged excitons in a monolayer semiconductor. *Nat. Commun.* **4**, 1474, <https://doi.org/10.1038/ncomms2498> (2013).
22. Berkelbach, T. C., Hybersten, M. S. & Reichman, D. R. Theory of neutral and charged excitons in monolayer transition metal dichalcogenides. *Phys. Rev. B* **88**, 045318, <https://doi.org/10.1103/PhysRevB.88.045318> (2013).
23. Ugeda, M. M. *et al.* Giant bandgap renormalization and excitonic effects in a monolayer transition metal dichalcogenide semiconductor. *Nat. Mater.* **13**, 1091–1095, <https://doi.org/10.1038/NMAT4061> (2014).
24. Gillen, R. & Maultzsch, J. Light–matter interactions in two-dimensional transition metal dichalcogenides: dominant excitonic transitions in mono- and few-layer MoX₂ and band nesting. *IEEE J. Sel. Top. Quantum Electron.* **23**, 219–230, <https://doi.org/10.1109/JSTQE.2016.2604359> (2017).
25. Ullah, F., Nguyen, T. K., Le, C. T. & Kim, Y. S. Pulsed laser deposition assisted grown continuous monolayer MoSe₂. *CrystEngComm* **18**, 6992–6996, <https://doi.org/10.1039/c6ce01392a> (2016).
26. Eda, G. *et al.* Photoluminescence from chemically exfoliated MoS₂. *Nano Lett.* **11**, 5111–5116, <https://doi.org/10.1021/nl201874w> (2011).
27. Tonndorf, P. *et al.* Photoluminescence emission and Raman response of monolayer MoS₂, MoSe₂, and WSe₂. *Opt. Express* **21**, 4908–4916, <https://doi.org/10.1364/OE.21.004908> (2013).
28. Ramakrishna Matte, H. S. S. *et al.* MoS₂ and WS₂ analogues of graphene. *Angew. Chem. Int. Ed.* **49**, 4059–4062, <https://doi.org/10.1002/anie.201000009> (2010).
29. Wilson, J. A. & Yoffe, A. D. The transition metal dichalcogenides discussion and interpretation of the observed optical, electrical and structural properties. *Adv. Phys.* **18**, 193–335, <https://doi.org/10.1080/00018736900101307> (1969).
30. Kang, J., Tongay, S., Zhou, J., Li, J. & Wu, J. Band offsets and heterostructures of two-dimensional semiconductors. *Appl. Phys. Lett.* **102**, 012111, <https://doi.org/10.1063/1.4774090> (2013).
31. Rakić, A. D. & Majewski, M. L. Modeling the optical dielectric function of GaAs and AlAs: Extension of Adachi’s model. *J. Appl. Phys.* **80**, 5909–5914, <https://doi.org/10.1063/1.363586> (1996).
32. Jellison, G. E. Jr. & Modine, F. A. Parameterization of the optical functions of amorphous materials in the interband region. *Appl. Phys. Lett.* **69**, 371–371, <https://doi.org/10.1063/1.118064> (1996).
33. Li, Y. *et al.* Measurement of the optical dielectric function of monolayer transition-metal dichalcogenides: MoS₂, MoSe₂, WS₂, and WSe₂. *Phys. Rev. B* **90**, 205422, <https://doi.org/10.1103/PhysRevB.90.205422> (2014).
34. Studna, A. A. *et al.* Lowretardance fusedquartz window for realtime optical applications in ultrahigh vacuum. *J. Vac. Sci. Technol. A* **7**, 3291, <https://doi.org/10.1116/1.576138> (1989).
35. Caramazza, S., Marini, C., Simonelli, L., Dore, P. & Postorino, P. Temperature dependent EXAFS study on transition metal dichalcogenides MoX₂ (X = S, Se, Te). *J. Phys.: Condens. Matter* **28**, 325401, <https://doi.org/10.1088/0953-8984/28/32/325401> (2016).
36. Çakır, D., Peeters, F. M. & Sevik, C. Mechanical and thermal properties of h-MX₂ (M = Cr, Mo, W; X = O, S, Se, Te) monolayers: A comparative study. *Appl. Phys. Lett.* **104**, 203110, <https://doi.org/10.1063/1.4879543> (2014).
37. Chernikov, A. *et al.* Exciton binding energy and nonhydrogenic Rydberg series in monolayer WS₂. *Phys. Rev. Lett.* **113**, 076802, <https://doi.org/10.1103/PhysRevLett.113.076802> (2014).
38. Savitzky, A. & Golay, M. J. E. Smoothing and differentiation of data by simplified least squares procedures. *Anal. Chem.* **36**, 1627–1639, <https://doi.org/10.1021/ac60214a047> (1964).
39. Cardona, M. *Modulation Spectroscopy*, Solid State Physics Supplement 11 (ed. Seitz, F., Turnbull, D. & Ehrenreich, H.) 9–87 (Academic Press, 1969).
40. Li, W. *et al.* Broadband optical properties of large-area monolayer CVD molybdenum disulfide. *Phys. Rev. B* **90**, 195434, <https://doi.org/10.1103/PhysRevB.90.195434> (2014).
41. Ho, C. H., Wu, C. S., Huang, Y. S., Liao, P. C. & Tiong, K. K. Temperature dependence of energies and broadening parameters of the band-edge excitons of Mo_{1-x}W_xS₂ single crystals. *J. Phys.: Condens. Matter* **10**, 9317–9328, <https://doi.org/10.1088/0953-8984/10/41/014> (1998).

Acknowledgements

This research was supported by Basic Science Research Program through the National Research Foundation of Korea (NRF) funded by the 'Ministry of Education' (NRF-2016R1D1A1B03931421) and supported by NRF grant funded by the 'Ministry of Science, ICT and Future Planning' (NRF-2016R1A2B1013734). This work was also supported by the 'In-line 3D-AFM for Nanodevices with 30 nm or less dimension (10051701)' Program, funded by the Ministry of Trade, Industry and Energy (MOTIE). One of authors (Y.S.K.) also thanks NRF grant (2009-0093818, 2014R1A4A1071686, 2017R1E1A1A01075350) for additional support. We thank D. E. Aspnes for useful discussions.

Author Contributions

H.G.P. and T.J.K. conceived the major part of the SE experiments. V.L.L. and H.T.N. performed data filtering. H.G.P., T.J.K., and Y.D.K. analyzed SE data. F.U. and Y.S.K. performed the synthesis and characterizations (OM, AFM, PL, and Raman). All authors were involved in writing the manuscript.

Additional Information

Supplementary information accompanies this paper at <https://doi.org/10.1038/s41598-018-21508-5>.

Competing Interests: The authors declare no competing interests.

Publisher's note: Springer Nature remains neutral with regard to jurisdictional claims in published maps and institutional affiliations.



Open Access This article is licensed under a Creative Commons Attribution 4.0 International License, which permits use, sharing, adaptation, distribution and reproduction in any medium or format, as long as you give appropriate credit to the original author(s) and the source, provide a link to the Creative Commons license, and indicate if changes were made. The images or other third party material in this article are included in the article's Creative Commons license, unless indicated otherwise in a credit line to the material. If material is not included in the article's Creative Commons license and your intended use is not permitted by statutory regulation or exceeds the permitted use, you will need to obtain permission directly from the copyright holder. To view a copy of this license, visit <http://creativecommons.org/licenses/by/4.0/>.

© The Author(s) 2018